Evidences of talc-white mica assemblage in low-grade metamorphic rocks from the Internal Zone of the Rif Cordillera (N Morocco)

Mª Dolores Rodríguez-Ruiz [a]*, Isabel Abad [b], María Bentabol [a], Mª Dolores Ruiz Cruz †

[a] *Departamento de Química Inorgánica, Cristalografía y Mineralogía, Facultad de Ciencias, Universidad de Málaga, Campus de Teatinos, s/n. 29071, Málaga, Spain*

[b] *Departamento de Geología y CEACTEMA, Universidad de Jaén, Campus Las Lagunillas s/n, 23071, Jaén, Spain*

*Corresponding author:
E-mail: mdrodriguez@uma.es
Avda. Louis Pasteur s/n
Campus de Teatinos
Facultad de Ciencias
Departamento de Química Inorgánica, Cristalografía y Mineralogía
Universidad de Málaga
29071, Spain

Abstract

Talc-phengite intergrowths were identified in epizone rocks from the Beni Mezala unit (Internal Zone of the Rif). These rocks show the non-common assemblage quartz-K-feldspar-albite-phengite-talc-vermiculite-chlorite/vermiculite mixed-layers. Although X-ray diffraction patterns indicate the presence of talc, talc could not be observed petrographically. In contrast, transmission electron microscopy indicates that white mica consists of nanometer-sized intergrowths of phengite and talc. At the scanning electron microscope scale, these micas show anomalously high contents of Fe+Mg composition (with an average value of 0.51 atoms per formula unit, *apfu*). The subtraction of the talc component from the mica formula allowed to obtain a mica with a limited phengitic substitution $K_{0.91}Na_{0.03}(Al_{1.74}Fe^{2+}_{0.23}Mg_{0.03}Ti_{0.03})_{\Sigma=2.03}(Si_{3.18}Al_{0.82})$ which permits an estimation of minimum pressure (*P*) <4 kbar. This is coherent with the medium-*P* facies series determinate by the *b*-cell parameter of white micas (9.036 Å). The detailed study at nanometer scale shows a domain structure of talc within the white mica packets probably originated by exsolution from a metastable precursor mica with high Fe+Mg contents. This has been interpreted as a relic of a H*P* assemblage in a low-grade metamorphic context. The study at nanometer scale should be considered as they may have petrological implications.

Key-words: Exsolution, phengite, talc, vermiculite, transmission-analytical electron microscopy.

Introduction

Many reactions can produce talc, a metamorphic sheet silicate, but most studies (either experimental or calculated) are limited to temperature (T) > 400 ˚C and P > 5 kbar. Specifically, the talc-phengite assemblage as an indicator of high-pressure (H*P*) metamorphism was first described and suggested by Abraham and Schreyer (1976) in piemontite-quartz schists from Serbia. Experimental and theoretical studies (Schreyer, 1985; Massonne and Schreyer, 1989; Wei and Powell, 2003, 2004) showed that the talc-phengite assemblage is stable under H*P* conditions (> 10 kbar), being very common in magnesian pelites from the Western Alps ("whiteschists"; Chopin, 1981), and in schists from the Sanbagawa belt, in southwest Japan (Izadyar et al., 2000; Ubukawa et al., 2007).

The most commonly described reactions leading to talc genesis at H*P* conditions are:

1. chlorite + phlogopite + quartz = talc + muscovite + H_2O
2. chlorite + quartz = talc + garnet + H_2O
3. chlorite + quartz = talc + chloritoid + H_2O
4. glaucophane + quartz = talc + albite + H_2O

But only Massonne and Schreyer (1989) proposed H*P* stability field for the theoretical talc-phengite assemblage.

Finding of the talc-phengite assemblage in pelitic rocks from Internal Zone units of the Rif (N Morocco) led to Bouybaouène (1993) and Bouybaouène et al. (1995), to deduce metamorphic conditions up to 550ºC/20 kbar. Nevertheless, the presence of the pumpellyite-actinolite assemblage and the composition of the several phases in veins from the Beni Mezala Unit indicated local metamorphic conditions as low as 280ºC/2 kbar (Ruiz Cruz et al., 2010), and suggested that other reactions should produce talc at lower grade conditions.

Most previously described talc+phengite-bearing rocks are schists with coarse-grained size (e.g. Ubukawa et al., 2007; Izadyar et al., 2014). Nevertheless, the talc-bearing rock from

the Rif are fine-grained (as shown below) and the study by classical petrographic methods (optical microscopy and electron microprobe, EMPA) was not possible or very limited. The results presented in this work are mainly based on a scanning and transmission electron microscopic study. The structural details of the talc-white mica intergrowths are considered under the perspective of a possible exsolution as it was already predicted by Veblen (1983) despite the more limited degree of solid solution of muscovite toward talc than that of wonesite. Numerous examples of exsolution in micas, at variable geological conditions, have been reported from the initial paper by Veblen (1983) showing as a consequence of the process a variety of intergrowths (e.g. Livi et al., 1997; Ferraris et al., 2000, 2001). Here, eventually, a plausible talc-forming mechanism is proposed, on the basis of the mineral assemblages and the textural relationships observed at the nanometer scale.

Geological setting

The Internal Zone of the Betic-Rif cordillera, the westernmost European Alpine chain (Fig. 1A), is formed of three tectonically superimposed complexes (Egeler and Simons, 1969), which are, from bottom upwards, the Nevado-Filábride, the Alpujárride (Betic)/Sebtide (Rif) and the Maláguide (Betic)/Ghomaride (Rif). The geotectonic relationships among the several complexes are essentially constant in the Betic-Rif cordillera: The Maláguide/Ghomaride complex tectonically overlies the Alpujárride/Sebtide complex, and this, the Nevado-Filábride complex, only present in the Betic Cordillera.

In addition, transitional units with tectonic positions intermediate between the Alpujárride/Sebtide and the Maláguide/Ghomaride complexes, and consisting of a set of thinned thrust slices, have been described in some areas of the cordillera (Didon et al., 1973; Sanz de Galdeano et al., 2001; Rodríguez-Ruiz et al., 2019). The sample used for this study was collected in the deepest unit of the Intermediate units: The Beni Mezala unit (Fig. 1). In the intermediate units (Federico units), the uppermost thrust slices show lithologic characteristics and metamorphic patterns similar to the Ghomaride complex, whereas increase in depth is characterized by the presence of intermediate lithologies and metamorphic patterns, and later

by lithologies and mineral assemblages typical of the Sebtide complex (Rodríguez-Ruiz et al., 2019).

After a detailed mineralogical study of these units (Rodríguez-Ruiz et al., 2019), the talc-phengite assemblage was only detected in the Beni Mezala unit. Three talc-free samples from the Beni Mezala unit (Table 1), also marked in Figure 1, have been used in this work for comparison.

The Triassic materials of the Beni Mezala unit (Fig. 1C) show a transition from dark schists, at the bottom, to blue phyllites with eruptive rocks according to Bouybaouène (1993), light calc-schists and carbonates, at the top. Talc-bearing rocks appear as several meters' thick light levels inter-bedded with typical blue phyllites, below the carbonate sequence. In contrast to phyllites, talc-bearing rocks are crumbly, although they show a schistose texture.

Sampling and Methodology

The intermediate units were sampled in the Beni Mezala antiform (Fig. 1B). A total of 40 samples were collected and a detailed mineralogical study have recently been published (Rodríguez Ruiz et al., 2019). For this work, four samples of the Beni Mezala unit were selected (Table 1), three of them were talc-free bearing rocks and only one of them was a talc-bearing rock. Although several samples have been selected, only the petrology of the talc-bearing rock is described in detail here. The talc-free samples (Fig. 1B; Table 1 and 2) have been used in this work to be able to establish a mineralogical and compositional comparison between both types of rocks (Table 1 and Table 2).

Samples were studied by petrographic microscopy, X-ray diffraction (XRD), X-ray fluorescence (XRF), scanning (SEM) and transmission-analytical electron microscopy (TEM/AEM).

The XRD patterns were recorded using a Philips X'Pert PRO MPD (University of Málaga), with CuKα_1 radiation and Ge monochromator, operated at 45 mA and 35 kV, with 0.01º2θ step size and 2 s counting time. Randomly oriented samples were used to determine the semi-quantitative principal mineral composition, using the diffraction peaks and intensity factors of Shultz (1964), and to deduce the *b*-cell parameter of white micas. Oriented, ethylene

glycol (EG) and heat treatment (550 ºC) of bulk, 2<ϕ<20 µm and <2 µm fractions were carried out to identify and establish the relative abundance of clay minerals composition, using the mineral intensity factors and reflection peaks of Islam and Lotse (1986) and Nieto (1983) and for determining the illite Kübler index (KI). This was measured as the width of the 10 Å peak at one-half maximum peak height of oriented <2 µm fraction expressed in $\Delta^{o}2\theta$ (Kübler, 1968), following the recommendations of Kisch (1991), and after transformation into Crystallinity Index Standardization (CIS) values (Warr and Rice, 1994) according to the equation y = 1.979x-0.073. The relative abundance of talc was determinated using the best intensity relation of the 001 diffraction peaks between the muscovite and talc in oriented, EG and heat treatment of bulk, 2<ϕ<20 µm and <2 µm fractions.

XRF analyses were carried out using a Philips Magix Pro PW 1040/10 spectrometer (Centro de Instrumentación Científica, CIC, University of Granada). Glass beads with lithium tetraborate were employed to minimise the preferential orientation of phyllosilicates. The detection limit for major elements is 0.01 *wt*. %. Ignition loss (LOI) was determined from 0.5 g of powdered sample, first dried at 110ºC and then heated at 1000ºC for one hour. The amount of the ferric iron in the selected samples was realized by titration (volumetric determination), which is consisted on sample dissolution by a hydrofluoric-sulphuric acid mixture.

Polished and carbon-coated thin sections corresponding to the talc-bearing sample were imaged using back-scattered electrons (BSE) using a ZEISS DSM 950 SEM, equipped with an X-ray energy dispersive (EDX) system (LINK QX 2000) at an accelerating voltage of 14 kV and 2nA beam current (CIC, University of Granada). A counting time of 100 s were used to analyze minerals in the SEM using the following standards: albite (Na), orthoclase (K), periclase (Mg), wollastonite (Si and Ca) and synthetic oxides (Al_2O_3, Fe_2O_3 and $MnTiO_3$). Moreover, a LEO 1430VP SEM with an EDX system, at an accelerating voltage of 20 kV and 1 nA beam current (CIC, University of Granada) was employed to obtained chemical mapping of several areas of interest.

Eventually, several areas with different textural characteristics, as described below, were selected from thin sections of the talc-bearing rock, and ion thinned for TEM/AEM study. Electron microscopy was performed at the University of Granada (CIC), with a 200 kV Philips

CM-20 transmission electron microscope, fitted with a scanning transmission device and solid-state detector for energy-dispersion analysis (EDX). Microanalyses were obtained in STEM mode using a raster of (0.10 × 0.02) μm in scanning mode to minimize alkali diffusion and volatilization with the long axis oriented parallel to the length of phyllosilicate packets. Counting times were 100 s except for Na and K, which were analyzed using counting times of 30 s to minimize alkali-loss problems as short counting times improve reproducibility for K and Na (Nieto et al., 1996). Quantitative determinations used the thin-film approximation of Cliff and Lorimer (1975). Albite (Na), muscovite and annite (K), albite, spessartine and muscovite (Al), forsterite and annite (Mg and Fe), spessartine (Mn) and titanite (Ca and Ti) were used as standards. Additionally, TEM images with higher resolution were obtained in a Jeol 3000 F, operated at 300 kV (Centro Nacional de Microscopía Electrónica, Complutense University of Madrid).

Results

Bulk-rock composition

As expected, differences among talc-bearing and talc-free samples from the Rif mainly affect to the relative MgO and FeO+Fe_2O_3 contents, with MgO/(FeO+Fe_2O_3) ratio close to 1 in the talc-bearing sample but around 0.25 in the talc-free samples (Table 2). When compared with talc-bearing samples from other localities (schists from the Alps and from Sanbagawa), the most notable feature in the Rif's samples is the higher K_2O contents, but in any case the values corresponding to different elements (wt.% oxides) show that the protolith of each talc-bearing sample is clearly different (Table 2).

X-ray data and petrography

Talc-bearing rock from the Beni Mezala unit is formed by sub-parallel, deformed brownish and light bands on the order of the millimeter scale, with very small grain size (< 20 μm; Fig. 2A). According to the XRD patterns (Fig. 2B; Table 1), it consists of quartz, K-feldspar, albite, white mica, chlorite-vermiculite mixed-layers, talc, and a poorly-ordered kaolinite-group mineral. No mineral typically associated to talc at H*P* conditions, such as chloritoid, garnet or glaucophane was identified in the talc-bearing rock.

The mixed-layer phase shows a broad integral reflection with d_{001} ~28.6 Å (Fig. 2B 1-2), which are scarcely affected by the treatment with EG, whereas clearly contract after heating at 550ºC (Fig. 2B 3). This behavior indicates the prevalence of a regular 1:1 chlorite/vermiculite mixed-layer (high-charge corrensite). Nevertheless, the notable decrease in intensity of the reflections of the mixed-layered phase after heating, coupled with the increase in intensity of the 10 Å reflection, suggest that discrete vermiculite is also present in the sample.

The KI is 0.24 Δº2θ in talc-bearing rock, and ranges from 0.23 to 0.27 Δº2θ in the other talc-free phyllites cited in this work. These values correspond to the epizone, according to the revised anchizone boundaries of the CIS scale (from 0.52 to 0.32 Δ°2θ, Warr and Ferreiro Mählmann, 2015). The *b*-cell value for potassic white mica in talc-bearing rock is 9.036 Å, while the *b*-cell value for potassic white mica in talc-free rocks included in this work ranges from 8.992 Å to 9.0228 Å.

SEM study

Back-scattered images (Figs. 2C and D) and EDX data (Fig. 2E) revealed that most brownish areas, as observed by petrographic microscopy (Fig. 2A), consist of very small, parallel potassic white mica grains, which contain abundant rutile inclusions, and K-feldspars; whereas the light areas consist of unoriented grains of several phases, including white mica, vermiculite, kaolinite-group minerals, quartz and idiomorphic grains of albite (Fig. 2D). Other scarcer dark bands (e.g. those observed at the upper left corner and the lower right corner of Fig. 2A) consist, however, of dominant trioctahedral chlorite-vermiculite mixed-layer. Since discrete grains of talc were not identified after an exhaustive examination of the thin sections, chemical mappings of several areas were also obtained. From the main clusters of chemical compositions, “mapping of phases” were also drawn. One of these is shown in the Figure 2E where blue areas correspond to the darkest areas in the Figure 2A (black arrows), and show the highest contents of Mg, although they also contain important amounts of Al. These Mg-rich areas are formed by sub-parallel grains of chlorite-vermiculite mixed-layers, which share the deformation features with the white mica-rich areas. The green areas correspond to white mica-rich brownish domains in Figure 2A, 2C and D. These areas contain, in addition, vermiculite (brown), abundant grains of rutile (white), which probably provides the brownish colour, and K-

feldspar (red). Light areas in Figure 2A, 2C and D consist of unoriented intergrowths of vermiculite, minor mixed-layers, albite (pink) and quartz (grey). Again, discrete talc grains were not identified, this fact suggesting that talc is intergrown with other phases under micrometer scale.

White mica formulae, calculated for 11 oxygens and assuming Fe as Fe^{2+} (Table 3), are characterized by very high Fe+Mg and low Al contents, coupled with octahedral occupancies >2 atoms per formula unit (*apfu*). Although calculations assuming Fe as Fe^{3+} lead to the decrease of the octahedral occupancy, the obtained values remain clearly >2 *apfu*. The interlayer content is usually < 0.90 *apfu*, showing a certain illitic substitution. In low-grade metamorphic rocks, white micas with high Fe+Mg contents, an excess of octahedral occupancy and interlayer deficiency are common and several substitutions might account for the deviations from the ideal K-white mica composition (Guidotti, 1984; Leoni et al., 1998; Abad et al., 2006). The influence of these possible substitutions on the composition of the white micas has been carefully examined. When analyses are plotted on a Si *vs.* Fe+Mg plot (Fig. 3A), it is evident that the Tschermak or celadonite substitution ($^{VI}Al^{IV}Al$, $^{VI}(Mg\text{-}Fe)_{-1}{}^{IV}Si_{-1}$) has scarce or null influence on the mica composition. Although some points plot near the line defining the ideal illitic substitution ($^{XII}K^{IV}Al$, $^{XII}\square_{-1}{}^{IV}Si_{-1}$) in the Figure 3B, most points plot far from this ideal line and do not show a defined trend. Figure 3C also reveals lack of the trioctahedral ($^{VI}(Fe+Mg)$,$^{XII}\square_{-1}$) substitution, proposed by Baldelli et al. (1989). In contrast, a well-defined trend is observed in the Fe+Mg vs. ^{VI}Al plot (Fig. 3D), indicating that the main substitution is $^{VI}Al_2{}^{VI}(Fe+Mg)_{-3}$, (biotitic substitution). Either this trend could, however represent true compositional variations or contamination by trioctahedral phases, this despite the analyzed grains were carefully selected.

Mappings of phases (Fig. 2E) indicate the presence, in addition to white mica, of two other populations of phyllosilicates with different Fe+Mg contents. The formulae of both types of phases were calculated assuming a vermiculitic composition for the Fe+Mg poorer and K richer phase (Table 4) and a chloritic composition for the Fe+Mg richer phase (Table 5). Despite the XRD patterns indicate that this latter phase is not true chlorite but chlorite-vermiculite mixed-layers, the formulae was calculated for 14 oxygens because some of the obtained analyses are close to trioctahedral chlorite corresponding to a clinochlore (Mg-rich) (Table 5, analyses 1-3).

Although the two populations cannot be directly compared, important variations in the composition of both types of phases have been observed (Fig. 4), suggesting the presence of submicroscopic intergrowths between both. The chemical trends shown in Figure 4, specially the parallel increase of Si and Al (Fig. 4A), and the negative correlation between (Fe+Mg) and Si (Fig. 4B), indicate that possible intergrowths of these phases with talc, if exist, must be very scarce.

TEM-AEM study

The study at nanoscale was carried out with three objectives: a) the general characterization of trioctahedral phases, b) to identify possible intergrowths of talc with the other phyllosilicates and c) to understand the anomalous composition of the white mica (Table 3). Despite trioctahedral phases are scarce in the talc-bearing rock, the identification at low magnification of chlorite-vermiculite mixed-layer has been possible due to the presence of lenticular gaps, reflecting contraction against the electron beam due to the vermiculitic component (Fig. 5A). The lattice-fringe images reveal that trioctahedral grains consist, in addition, of finer intergrowths of packets with basal spacing of ~24 Å and packets with basal spacing of ~10 Å, interpreted as corresponding to regular 1:1 chlorite-vermiculite sequences and discrete vermiculite (Fig. 5B). The AEM data of these areas show, as expected, notable variations, according to the relative content of mixed-layers and vermiculite. Although the analyses of the mixed-layer phases have been now recalculated for 25 oxygens (Table 6, analyses 1-5), the interlayer content varies from 0.17 to 0.73 *apfu*, indicating that the relative content of vermiculite and chlorite varies considerably even at the nanometer scale. In addition, some of the obtained analyses provide structural formulae typical of phlogopite (Table 6, analyses 6-7), some of them with Na contents almost similar to K contents. The vermiculite formulae (Table 6, analyses 8-14) also show important chemical variations, although they indicate a dioctahedral nature; the octahedral occupancy, clearly >2 *apfu* suggests, however, that some Mg probably occupies the interlayer positions. As at the SEM scale, the formulae of this mineral, obtained at the TEM scale, indicate lack of talc contribution.

Low-magnification images of the white mica grains also reveal the presence of fine intergrowths of several phases: the most frequent intergrowths consist of white mica ($2M_1$

polytype) and thinner vermiculite packets, which are rapidly damaged (Fig. 5C). Intergrowths of white mica, vermiculite, and mixed-layers are also frequent (Fig. 5D). Although the SAED patterns obtained from large mica grains show, in some cases (Fig. 5D, inset), reflections which could be ascribed to talc, this adscription is not sure, since mica is intergrown with other phases. As observed at higher magnification, the damaged areas show 10 Å basal spacing (Fig. 5E), and AEM data typical of a dioctahedral phase, with high Si content up to 3.31 *apfu* and low interlayer content in some cases (values around 0.6-0.7 *apfu*, Table 7). Unoriented grains (Fig. 2C-D) consist, in addition to mica and vermiculite grains, of spherical morphologies characteristic of halloysite (Fig. 5F), and planar packets with 7 Å basal spacing correspond to kaolinite (Fig. 5G). White mica formulae, as deduced from the AEM data (Table 7), again show octahedral occupancies >2 *apfu*, but lower Si contents, and higher Na contents than those deduced from the analyses obtained at the SEM scale (Table 3). Discrepancies among both datasets are probably due to the greater homogeneity of the areas studied by TEM, and to some volatilization, as indicated by the low interlayer charge in some formulae.

The lattice-fringe images of the mica packets show the characteristic mottled aspect of the potassic white mica. In a great extent, the contrast effects are due to the presence of small packets of layers with light contrast, the density of which is variable from grain to grain (Fig. 6). These lens-shaped packets show, in some areas, a rough organisation, in bands on the order of few hundred angstroms, oblique by respect of the basal plane, which remember talc exsolutions in wonesite, described by Veblen (1983). Although the Fourier transform (FT) images do not show discrete talc reflections, streaking of the basal reflections parallel to c* is evident (Fig. 6, inset A). In addition, the EDX spectra included in Figure 6 show a Si and Mg increase and an Al and K decrease in the mica packets with higher density of light areas (spectrum at the bottom), suggesting talc contribution, if comparing with the spectrum at the top from the mica packets with less light areas. The maximum angle measured between the lamellae and 001 of mica is ~35º, near the 37º found by Veblen (1983). The FT images (Fig. 6, inset B) suggest that average orientations are close to [11 $\bar{6}$] and [$\bar{1}$1 $\bar{6}$], although there is an ambiguity in orientation mainly resulting from the irregular shape of the talc lamellae and from the difficulty for obtaining images with variable orientations.

The [100] or equivalent images obtained at higher magnification (e.g. Fig. 7A) reveal that these areas consist of dark domains where ordered 2-layers mica which coexists with areas where one of each two mica layers appears to have lost the interlayer sheet, by comparing with the images of Murakami et al. (2003). Light domains consist of layers which are, in appearance, rotated with respect to the mica layers, in such a way that c* axis of these domains is not contained in the plane of the image. The presence of the mixed-layer structure has also been revealed by the FT image (Fig. 7A, inset). In contrast, irregular and curved light domains (Fig. 8) intergrown with perfectly ordered 2-layer mica (Fig. 9A), whereas talc-mica interstratifications are lacking, according to the FT images (Fig. 8, inset). Only occasionally, the HRTEM images permitted the observation of 9.3 Å talc fringes, showing a common orientation with mica (Fig. 9B). Some bending of layers is observed associated to these areas (Figs. 8, Talc zone, and 9B). The size of the several domains prevents the obtaining of accurate chemical data. Nevertheless, the AEM data obtained from larger areas, although influenced by the volatilization of K, show Mg contents up to 0.57 *apfu*, coupled with high octahedral occupancies (Table 7). All these data suggest that talc forms a domain structure within the white mica packets.

Based on an average mica:talc ratio ~10:1, as deduced from the XRD patterns (Fig. 2B), the talc component was subtracted from the average mica formula obtained at the SEM scale ($K_{0.82}Na_{0.03}(Al_{1.59}Mg_{0.31}Fe^{2+}_{0.20}Ti_{0.03})_{\sum 2.12}(Si_{3.26}Al_{0.74})$), assuming that talc only contains Mg, although the EDX data indicated that talc-rich areas also contain certain amount of Fe (Fig. 6, spectrum at the bottom). The recalculated mica formula is $K_{0.91}Na_{0.03}(Al_{1.74}Fe^{2+}_{0.23}Mg_{0.03}Ti_{0.03})_{\Sigma=2.03}(Si_{3.18}Al_{0.82})$, which corresponds to a white mica with limited phengitic substitution.

Discussion

Talc-white mica intergrowths identification

Previous studies of the rock-type studied in this work described “talc-phengite” grains, assuming that talc and phengite were intergrown at a submicroscopic scale (Bouybaouène, 1993). But as described in the Results section, despite the deep textural and chemical study at the SEM scale (BSE images and chemical analyses), discrete talc grains were not found in talc-

bearing samples in spite of the information given by the XRD patterns (Fig. 2B). It seems then evident that talc should be only present as nanometer-sized domains within the white mica. Ferraris et al. (2000) detected talc within apparently pure white micas as nanometer-sized domains, but talc was also presented as flakes overgrowing large phengite crystals at micrometer scale. In addition, TEM research about talc-phengite relationships (e.g. Ferraris et al., 2000; Curetti et al. 2018) that include a polytype characterization show that the phengite polytype is 3*T*, which is the usual polytype under high-pressure conditions. This is not the case of the studied phengites here, characterised by a $2M_1$ polytype (SAED Fig. 5C). Although the SAED patterns show frequently splitting of the basal reflections, only mica and mica/talc reflections were generally observed in the FT images of the talc-rich areas, probably due to the fact that the talc domains are not perfectly oriented with respect to mica.

Some HRTEM images (Figs. 7 and 9) indicate that the TOT layers are continuous in mica and talc, that is, the talc-white mica intergrowth is coherent. The misfit caused by the difference in the basal spacings of talc (9.3 Å) and white mica (10 Å) has been, in appearance, resolved by several coupled mechanisms: small rotation and bending of the layers, and presence of transitional domains with an intermediate structure between talc and mica. Although the exact determination of the orientation of the talc lattice in the lamellae is difficult, if the talc lamellae are parallel to [11 $\bar{6}$] and [$\bar{1}$1 $\bar{6}$] of mica, these planes can be almost coincident with [11 $\bar{3}$] and [$\bar{1}$1 $\bar{3}$] of talc. This relative orientation would require a small rotation of the a*- and b*-axis in addition to c*.

These observations suggest that talc-white mica intergrowths are the result of an exsolution from a metastable precursor of dioctahedral micas with higher Fe+Mg contents than the expected values in a “true” dioctahedral mica. From the initial paper by Veblen (1983), numerous examples of exsolution in micas, at very variable geological conditions, have been reported. The exsolution processes in micas lead, in addition, to a variety of intergrowths, including only trioctahedral phases (Veblen, 1983), di- and trioctahedral phases (Ferrow et al., 1990; García-Casco et al., 1993; Ferraris et al., 2001), or dioctahedral phases (Livi et al., 1997). The degree of solid solution of muscovite toward talc is notably more limited than that of wonesite, but the possible presence of exsolutions such as that described here was already

predicted by Veblen (1983). Nevertheless, the size of the talc domains described here (< 200 Å) are notably smaller, and these present, in addition, less regularity than other exsolution textures that could be observed at the scale of the petrographic microscope (e.g. García Casco et al, 1993; Ferraris et al., 2001; among others). The orientation of the talc domains would favor the diffusion parallelly to the layers during exsolution, as also pointed out by Veblen (1983), as well as the fitting between the 001 planes of both lattices by means of very small rotation of the layers. The case studied here allows to state that it is evident that the TEM study permits the identification of exsolution textures with lower sizes (even a few tens of Å), suggesting that the generalized use of this technique possibly will show that exsolution in micas is a process more common than previously assumed.

Mineral assemblages and origin of talc-bearing rocks

The mineral assemblage (white mica + talc + vermiculite + chlorite/vermiculite mixed layers) has not been previously described in Triassic sequences from the Internal Zone of the Betic-Rif range and is a very rare one in pelitic rocks. Indeed, light rocks as the whitish schist MG-18 with this unusual mineral assemblage and inter-bedded with blue phyllites, which show the usual muscovite+chlorite assemblage (Table 1), are very scarce. Although the composition of the white mica, after subtracting the talc component, is in accordance with the composition of white micas from other rocks of the same unit, as the talc-free samples (e.g. blue phyllites; see Rodríguez-Ruiz et al., 2019 for more information) selected for this research the absence of chlorite and the presence instead of chlorite-vermiculite mixed-layers and vermiculite, suggest that both chemical differences (mainly MgO contents, Table 2) and mineralogical ones are probably related to differences in the nature of their protoliths. In fact, in the Triassic sequences of the Intermediate units have been described different kinds of rocks (limestone, marbles, low-grade metamorphic clastic rocks, eruptive rocks, among others; e.g. Bouybaouène, 1993; Chalouan et al., 2008). Moreover, the presence of phlogopites (Table 7) and very abundant rutile grains included in the large white mica areas (Fig. 2E), which suggests that these could derive from a Ti-rich phase (phlogopite?), points to a magmatic origin for the whitish schist whereas a sedimentary origin is more plausible for the blue phyllites.

In the studied rocks, Na is in very low amounts, and mainly concentrated in albite. Ca is also in very low amounts and concentrated in vermiculitic phases. Thus, neglecting these components, the mineral assemblages can be analysed in the Al_2O_3-(K,Na)AlO_2-(Fe_{total},Mg,Mn)O plane, from the H_2O, quartz, and albite apices, in order to show the main compositional relations between the several phases (Fig. 10A). Although mica analyses display a phengitic trend, they are placed far from the line defining the ideal phengitic substitution. As well, analyses of the chlorite-vermiculite mixed-layers plot near the field of typical chlorite, and vermiculite is placed at intermediate position between white mica and chloritic phases. The position of some vermiculite points also suggests that these are mixed analyses of vermiculite and chlorite/vermiculite mixed-layers.

The current assemblage of the talc-bearing rocks in this research is probably the result of a complex metamorphic history as a consequence of successive stages of recrystallization. This is also the case of the talc-bearing schists from the Alps, where a sedimentary (Schreyer, 1977; Chopin, 1981) and a metasomatic (Bearth, 1952; Compagnoni and Lombardo, 1974; Compagnoni and Hirajima, 1992) origin have been proposed, although the nature of the phengite polytype differs from our case.

A tentative evolution of the mineral composition of our talc-bearing rocks has been graphically represented in Figure 10B. According to Chopin (1981), usual pelitic compositions may be expressed as a mixture of quartz, chlorite and illite, in the *KFMASH* system. In our case, since textural images (Fig. 2C-E) suggest that unoriented grains such as kaolinite-group minerals and vermiculite are retrogressive phases formed after the main deformation stage, we can start from the average mica composition shown in Table 3 (M1, in Figure 10B) and from the average chlorite/vermiculite mixed-layers composition, shown in Table 5 (ML, in Figure 10B). These two phases would define an initial assemblage (1 in Figure 10B). Mica with composition M1, and perhaps chlorite-vermiculite mixed-layers (assemblage 1), must have formed under non-equilibrium conditions. Probably, an approach to the equilibrium, leading to the exsolved mica+talc assemblage (2 in Figure 10B), occurred during the first stage, high pressure/low temperature episode (Azañón and Goffé, 1997), of the alpine metamorphic event. The

possibility that this process occurred during the H*T* episode associated to decompression can be discarded, given the phengitic nature of the exsolved white mica.

The determined Fe+Mg contents in the micas of this work contrast with the value of *b*-cell measured. Using several models and equations (Grim et al., 1951; Radoslovich, 1962; Radoslovich and Norrish, 1962; Cipriani et al., 1968), it can be deduced that for Fe+Mg contents on the order of 0.51 *apfu* (range for Fe+Mg contents: 0.31-0.70 *apfu*), which are values frequently found in the mica here analysed, the expected *b*-cell values would range from 9.056 to 9.062 Å. In contrast, white mica from talc-bearing rock shows a *b*-cell value of 9.036 Å; so, considering these data the white mica composition clearly points to contamination by a trioctahedral phase. According to these results, it seems evident that the composition of white mica (^{IV}Si and/or ^{VI}(Fe+Mg) contents) from the talc-bearing rock, as deduced from EDX data obtained at the SEM scale, cannot be used for estimating the *P* range in which the white mica formed. Although the slope of the Si isopleths for phengite are dependent on mineral assemblages, in the range of *T* estimated for this unit (280-400ºC) from previous works at pumpellyite-bearing assemblages (Ruiz Cruz et al., 2010), the Si content rises linearly, according to Massonne and Schreyer (1987), and average mica composition (Table 3) would indicate minimum *P* between 4.5 and 6 kbar. Nevertheless, the estimated minimum *P* becomes <4 kbar when the talc component is subtracted from the white mica formula which is coherent with the medium-*P* facies series determinate by the *b*-cell parameter of white micas (9.036 Å), according to Guidotti and Sassi (1986).

Conclusions

Textures and structural and chemical details of the white mica-talc intergrowths found in rocks from the Northern Rif indicate that an apparent Fe+Mg-rich, probably metastable white mica is in fact a lamellar intergrowth of phengite and talc. The nanometer-sized talc domains present in phengite provide an example of a relic of a H*P* assemblage in a low-grade metamorphic context. This work also reveals that, although X-ray diffraction is the more reliable technique for detecting small amounts (abundance < 10%) of talc or other minoritary phyllosilicates, these types of intergrowths can only be identified by TEM/AEM.

The talc-phengite assemblage described here, although probably formed during the high-pressure/low-temperature alpine metamorphic event, points to pressures on the order of 4 kbar, in accordance with conditions previously deduced from pumpellyite-bearing assemblages. Then, this research demonstrates that white mica with high Si contents does not necessarily reflects high pressures of formation, characteristic of the most of the described talc-phengite assemblages, and raises the possibility that some of such “phengites”, as determined from the more common microprobe technique, may contain small volumes of talc as identified by X-ray diffraction.

Acknowledgements

The authors are grateful to J.L. Baldonedo and A. Gómez from the National Electron Microscopy Center of the Complutense University of Madrid and M.M. Abad from the Centro de Instrumentación Científica of the University of Granada for help with HRTEM work. Authors are also grateful to C. Sanz de Galdeano for his helpful in the fieldwork and the anonymous referee, whose suggestions improved the quality of the manuscript.

This research has been funded by Research Project CGL2009-08186 (Spanish Ministery of Education and Science) and PGC2018-094572-BI00 (MCIU/AEI/FEDER, EU) and Research Groups RNM-199 and RNM-325 of the Junta de Andalucía.

References

Abad, I.; Nieto, F.; Gutiérrez-Alonso, G.; Do Campo, M.; López-Munguira, A.; Velilla N., 2006. Illitic substitution in micas of very low-grade metamorphic clastic rocks. Eur. J. Mineral. 18, 59-69.

Abraham, K.; Schreyer, W., 1976. A talc-phengite assemblage in piemontite schist from Brezovica, Serbia, Yugoslavia. J. Petrol. 17, 421-439.

Azañón, J.M.; Goffé, B., 1997. Ferro- and magnesiocarpholite assemblages as record of high-P, low-T metamorphism in the Central Alpujárrides, Betic Cordillera (SE Spain). Eur. J. Mineral. 9, 1035-1051.

Baldelli, C.; Franceschelli, M.; Leoni, L.; Memmi, I., 1989. Ferrimuscovite and celadonite substitutions in muscovite from Fe^{3+}-rich low-grade psammitic rocks (Northern Apennines, Italy). Lithos 23, 201-208.

Bearth, P., 1952. Geologie und Petrographie des Monte Rosa. Beitr. Geol. Karte der Schweiz. Lf. 96, 1-94.

Bouybaouène, M.L., 1993. Étude petrologique des metapelites Sebtides superieures, Rif Interne, Maroc: Une évolution metamorphique de haute pression. Ph. Thesis. Université Mohammmed V, Rabat, 151 pp.

Bouybaouène, M.L.; Goffé, B.; Michard, A., 1995. High pressure, low-temperature metamorphism in the Sebtides nappes, northern Rif, Morocco. Geogaceta 17, 117-119.

Chalouan, A.; Michard, A.; El Kadiri, Kh.; Negro, F.; Frizon de Lamotte, D.; Soto, J.I.; Saddiqui, O., 2008. The Rift Belt. In Michard, A., Saddiqui, O., Chalouan, A., Frizon de Lamotte (eds). Continental evolution: The Geology of Morocco. Lect. Notes Earth Syst. Sci. 203-302.

Chopin, C., 1981. Talc-phengite: A widespread assemblage in high-grade pelitic blueschists of the western Alps. J. Petrol. 22, 628-650.

Cipriani, C.; Sassi, F.P.; Viterbo-Bassani, C., 1968. La composizione delle miche chiare in rapport con le constant reticolari e col grado metamorfico. Rend. Soc. Ital. Mineral. Petrol. 24, 153-187.

Cliff, G.; Lorimer, G.W., 1975. The quantitative analysis of thin specimen. J. Microsc. 103, 203-207.

Compagnoni, R.; Lombardo, B., 1974. The Alpine age of the Gran Paradiso eclogite. Rend. Soc. Ital. Mineral. Petrol. 30, 223-237.

Compagnoni, R.; Hirajima, T., 1992. Occurrence and significance of superzoned garnet in the coesite-bearing whiteschist of southern Dora-Maira Massif, western Alps. A599 29th Int. Geol. Conf. Kyoto, Japan.

Curetti, N. ; Bonadiman, C. ; Compagnoni, R. ; Nodari, L. ; Corazzari, I. ; Pavese, A., 2018. Phengite megacryst *quasi*-exsolving phlogopite, from Sulu ultra-high pressure metamorphic terrane, Qinglongshan, Donghai County (eastern China) : New data for *P-T-X* conditions during exhumation. Lithos 314-315, 156-164.

Didon, J.; Durand-Delga, M.; Kornprobst, J., 1973. Homologues géologiques entre les deux rives du Detroit de Gibraltar. B. Soc. Geol. Fr. 15, 77-105.

Egeler, C.G.; Simons, O.J., 1969. Sur la tectonique de la Zone Bétique (Cordillères Bétiques, Espagne). Verh. Kon. Ned. Akad. Wetensch. Natuurk. 25, 3-90.

Ferraris, C.; Chopin, C.; Wessicken, R., 2000. Nano- to micro-scale decompression products in ultrahigh-pressure phengite : HRTEM and AEM study, and some petrological implications. Am. Mineral. 85, 1195-1201.

Ferraris, C.; Grobety, B.; Wessicken, R., 2001. Phlogopite exsolutions within muscovite: a first evidence for a higher-temperature re-equilibration, studied by HRTEM and AEM techniques. Eur. J. Mineral. 13, 15-26.

Ferrow, E.A.; London, D.; Goodman, K.S.; Veblen, D.R., 1990. Sheet silicates of the Lawler Peak granite, Arizona: chemistry, structural variations and exsolution. Contrib. Mineral. Petr. 105, 491-501.

García-Casco, A.; Sánchez-Navas, A.; Torres-Roldán, R.L., 1993. Disequilibrium decomposition and breakdown of muscovite in high P-T gneisses, Betic alpine belt (southern Spain). Am. Mineral. 78, 158-177.

511 Grim, R.E.; Bradley, W.C.; Brown, G., 1951. The mica clay minerals. In: Brindley, G.W. (Ed) X-
512 ray identification and crystal structure of the clay minerals. Min. Soc. London, pp. 138-
513 172.
514 Guidotti, C.V., 1984. Micas in metamorphic rocks. Rev. Mineral. 13, 357-467.
515 Guidotti, C.V.; Sassi, F.P., 1986. Classification and correlation of metamorphic facies series by
516 means of muscovite b_o data from low grade metapelites. Neues Jb. Miner. Abh. 153,
517 363-380.
518 Islam, A.K.M.E.; Lotse E.G., 1986. Quantitative mineralogical analysis of some Bangladesh
519 soils with X-Ray, Ion exchange and selective dissolution techniques. Clay Miner. 21, 31-
520 42.
521 Izadyar, J.; Hirajima, T.; Nakamura, D., 2000. Talc-phengite-albite assemblage in piemontite-
522 quartz schist of the Sanbagawa metamorphic belt, central Shikoku, Japan. Isl. Arc 9,
523 145-158.
524 Izadyar, J.; Mojab, S.; Kuroshi, O; Zare, M., 2014. An unusual assemblage of talc-penghite-
525 chlorite-K-feldspar in quartz schist from the Nahavand area, Sanandaj-Sirjan zone, Iran.
526 Iran. J. Sci. Technol. Trans. 38A3, 243-252.
527 Kisch, H.J., 1991. Illite crystallinity; recommendations on sample preparation, X-ray diffraction
528 settings, and interlaboratoy samples. J. Metamorph. Geol. 9, 665-670.
529 Kübler, B., 1968. Evaluation quantitative du métamorphisme par la cistallinité de l'illite. Etat des
530 progrès réalisés ces dernières années. Bull. Cent. Rech. Pau SNPA 2, 385-397.
531 Leoni, L.; Sartori, F.; Tamponi, M., 1998. Compositional variation in K-white micas and chlorites
532 coexisting in Al-sarurated metapelites under late diagenetic to low-grade metamorphic
533 conditions (Internal Liguride Units, Northern Apennines, Italy). Eur. J. Mineral. 10, 1321-
534 1339.
535 Livi, K.J.T.; Veblen, D.R.; Ferry, J.M.; Frey, M., 1997. Evolution of 2:1 layered silicates in low-
536 grade metamorphosed Liassic shales of Central Switzerland. J. Metamorph. Geol. 15,
537 323-344.
538 Massonne, H.J.; Schreyer, W., 1987. Phengite geobarometry based on the limiting assemblage
539 with K-feldspar, phlogopite, and quartz. Contrib. Mineral. Petr. 96, 212-224.

Massonne, H.J.; Schreyer, W., 1989. Stability field of the high-pressure assemblage talc-phengite and two new phengite barometers. Eur. J. Mineral. 1, 391-410.

Murakami, T.; Utsunomiya, S.; Yokohama, T.; Kasama, T., 2003. Biotite dissolution processes and mechanisms in the laboratory and in nature: early stage weathering environment and vermiculitization. Am. Mineral. 88, 377-386.

Nieto, F., 1983. Las cloritas de las Cordilleras Béticas. Ph Thesis, Universidad de Granada, Granada, 249 pp.

Nieto, F.; Ortega-Huertas, M.; Peacor, D.R.; Arostegui, J., 1996. Evolution of illite/smectite from early diagenesis through incipient metamorphism in sediments of the Basque-Cantabrian Basin. Clays Clay Miner. 44, 304–323.

Radoslovich, E.W., 1962. The cell dimensions and symmetry of layer-lattice silicates: II. Regression relations. Am. Mineral. 47, 617-636.

Radoslovich, E.W.; Norrish, K., 1962. The cell dimensions and symmetry of layer-lattice silicates: I. Some structural considerations. Am. Mineral. 47, 599-616.

Rodríguez-Ruiz, M.D.; Abad, I.; Bentabol, M.J., 2019. Permo-Triassic clastic rocks from the Ghomaride complex and Federico Units (Rif Cordillera, N Morocco): An example of diagenetic-metamorphic transition. Minerals 9, 738, https://doi:10.3390/min9120738.

Ruiz Cruz, M.D.; Sanz de Galdeano, C.; Álvarez-Valero, A.; Rodríguez Ruiz, M.D.; Novak, J., 2010. Pumpellyite and coexisting minerals in metapelites and veins from the Federico Units in the Internal Zone of the Rif, Spain. Can. Mineral. 48, 183-203.

Sanz de Galdeano, C.; Andreo, B.; García-Tortosa, F.J.; López Garrido, A.C., 2001. The Triassic palaeogeographic transition between the Alpujárride and Maláguide complexes, Betic-Rif Internal Zone. Palaeogeogr. Palaeocl. Palaeoecol. 167, 157-173.

Schreyer, W., 1977. Whiteschists: Their compositions and pressure temperature regimes based on experimental, field and petrographic evidence. Tectonophysics 43, 127-144.

Schreyer, W., 1985. Metamorphism of crustal rocks at mantle depth: High-pressure minerals and mineral assemblages in metapelites. Fortschr. Mineral. 63, 227-261.

Schultz, L.G., 1964. Quantitative interpretation of mineralogical composition from X-ray and chemical data for the Pierre Shale. Analytical methods in geochemical investigations of

569 the Pierre Shale. U.S. Geological Survey, Washington D.C., USA, Professional Paper
570 391-C, 1-31.
571 Ubukawa, T.; Hatanaka, A.; Matsumoto, K.; Hirajima, T., 2007. Pseudosection analysis for talc-
572 Na pyroxene-bearing piemontite-quartz schist in the Sanbagawa Belt, Japan. Isl. Arc
573 16, 553-574.
574 Veblen, D.R., 1983. Exsolution and crystal chemistry of the sodium mica wonesite. Am. Mineral.
575 68, 554-565.
576 Warr, L.N.; Rice H.N., 1994. Interlaboratory standardization and calibration of clay minerals
577 crystallinity and crystallite size data. J. Metamorph. Geol. 12, 141-152.
578 Warr, L.N.; Ferreiro-Mählmann, R., 2015. Recommendations for Kübler Index standardization.
579 Clay Miner. 50, 283-286.
580 Wei, Ch.; Powell, R., 2003. Phase relations in high-pressure metapelites in the system
581 KFMASH (K_2O-FeO-MgO-Al_2O_3-SiO_2-H_2O). Contrib. Mineral. Petrol. 145, 301-315.
582 Wei, Ch.; Powell, R., 2004. Calculated phase relations in high-pressure metapelites in the
583 system NKFMASH (Na_2O-K_2O-FeO-MgO-Al_2O_3-SiO_2-H_2O). J. Petrol. 45, 183-202.
584 Whitney, D.L.; Evans, B.W., 2010. Abbreviations for names of rock-forming minerals. Am.
585 Mineral. 95, 185-187.
586

587 **Figures**

588 **Figure 1.** A: location of the Betic-Rif orogen and the studied area (red asterism) in the
589 Mediterranean Sea. B: geological map of the Rif area next to Ceuta. The samples cited in this
590 work and plotted in this map are the talc-bearing sample MG-18 (N35º54'46.6''W0.5º22'35'')
591 and the talc-free samples: MG-14 (N35º54'36.4''W5º22'29.1''), MG-62
592 (N35º52'23.4''W5º23'26.7''), and MG-64 (N35º52'09.4''W5º23'08.2''). C: Stratigraphic column
593 corresponding to the Beni Mezala unit, indicating with a red arrow the relative position of the
594 talc-bearing sample (MG-18).

595 **Figure 2.** A: microscopic image (parallel nicols), corresponding to the talc-bearing sample. The
596 darkest areas are the mixed-layer-rich areas (black arrows). B: XRD patterns from oriented
597 samples (1, air-dried; 2, EG and 3, 550ºC) showing the current mineral assemblage in the talc-
598 bearing sample. The basal reflections of chlorite-vermiculite mixed-layers (ML) are indexed and
599 numbers indicate basal spacing values. Ms: white mica; Tlc: talc; Hal: halloysite; Ab: albite; K-fs:
600 K-feldspar; Qz: quartz. C: BSE image showing a detail of the talc-bearing samples texture. D:
601 unoriented aggregates of dominant vermiculite, and minor white mica and albite (light areas in
602 image A). E: mapping of phases corresponding to the square in image A, based on the main
603 compositional populations. Ms: green; ML: blue; vermiculite (Vrm): brown; Ab: pink; Kfs: red;
604 rutile (Rt): white; Qz: grey. Mineral symbols in all figures according to Whitney and Evans
605 (2010).

606 **Figure 3.** Chemical plots showing the main trends in white mica of talc-bearing rock.
607 Continuous lines correspond to the ideal celadonitic substitution (A), illitic substitution (B),
608 trioctahedral substitution (C) and biotitic substitution (D). Discontinuous line: regression line.

609 **Figure 4.** Plots of the chemical composition of chlorite-vermiculite mixed-layers (squares)
610 (formulae calculated for 14 oxygens), and vermiculite (crosses) (formulae calculated for 11
611 oxygens) of talc-bearing rock. A: Si *vs.* Al; B: Si *vs.* Fe; C: Si *vs.* ∑oct.; D: Si *vs.* ∑ Int.

612 **Figure 5.** TEM images of the main phases present in talc-bearing rocks. A: white mica and
613 vermiculitic phases showing lenticular gaps. The SAED pattern (inset) shows ~10 Å periodicity.
614 B: lattice-fringe image showing fine intergrowths of damaged vermiculite and chlorite-vermiculite
615 mixed-layers; reflections of both phases in SAED pattern (inset). C: intergrowths of white mica

and vermiculitic packets. The SAED pattern viewed along [100] (inset) corresponds to a two-layers mica polytype. D: intergrowth of white mica, vermiculite and chlorite-vermiculite mixed-layer packets; splitting of the basal reflections in the SAED pattern (inset). E: lattice-fringe images of damaged vermiculite packets intergrown with white mica. F: secondary phases mainly consist of packets and spheres of halloysite (Hal; and kaolinite?) and Fe-oxide. G: Lattice-fringe image of kaolinite or halloysite packets (7 Å) intergrown with white mica (10 Å). Numbers correspond to analyses reported in Tables 6 and 7.

Figure 6. Lattice-fringe images of two mica grains showing variable density of light areas. The EDX spectra obtained at both sides of the grain boundary (inset) show very slight variations in composition, mainly affecting to Si, Al, Mg and K. The white lines indicate the approximate orientation of the light areas. The FT image (inset A) shows streaking of the basal reflections parallel to c*, suggesting contribution of talc and mica. The possible orientations of the lamellae are marked in inset B.

Figure 7. A: [1 $\bar{1}$0] HRTEM image showing a set of white mica and discontinuous talc lamellae. The apparent orientation of the lamellae (11 $\bar{6}$) has been labelled in the FT image (inset). This image shows moreover, 00*l* reflections with ~20 Å spacing, interpreted as corresponding to regular alternation of white mica and talc layers superimposed to the mica reflections. B: schematic interpretation of the right side of the HRTEM image.

Figure 8. [1 $\bar{1}$0] HRTEM image obtained from an area with high density of light fringes, revealing that consist of domains of perfectly ordered mica with a two-layers structure including irregular domains with a bad-defined structure. These latter are generally limited by slightly curved fringes (arrows). The FT image corresponds only to ordered two-layers mica structure.

Figure 9. Details of some areas from Figure 8. A: perfectly ordered two-layers sequence in white mica domains. B: domains where apparent loss of the interlayer cations leads to fringes with ~9.3 Å associated to a domain with, in appearance, disordered structure (Tlc zone in Figure 8).

Figure 10. A: mineral assemblages of talc-bearing rocks on the Pyrophyllite – K-feldspar – Talc diagram (plus quartz, albite and H_2O). B: tentative evolution of the mineral assemblages based on mean compositions of the several phases. WR: Whole rock XRF composition.

Highlights:

- Talc-white mica assemblage in low-grade metamorphic rocks
- Talc-phengite intergrowth from a metastable precursor mica with high Fe+Mg contents
- Importance of the HR-TEM for identification of talc-phengite and other intergrowth
- Qz-Kfs-Ab-Ph-Tlc-Vrm-C/V ML assemblage as non-common talc-phengite-bearing rock

Table 1

Click here to download Table: Table 1.docx

Table 1. Location, lithology and semi-quantitative mineralogical composition of whole rock and clay fraction (<2 μm) of Beni Mezala samples. Mineral abbreviations, Qz: quartz; Kfs: K feldspar group mineral; Pl: plagioclase group mineral; Phy: phyllosilicates; Ms: muscovite/phengite; Pg: paragonite; Prl: pyrophyllite; Tlc: talc; Chl: chlorite; Vrm: vermiculite; C/V: mixed-layers chlorite/vermiculite; Kln: kaolinite group mineral.

Sample	Location	Lithology	Whole rock					< 2μm size-fraction							
			Qz	Kfs	Pl	Others	Phy	Ms	Pg	Prl	Tlc	Chl	Vrm	C/V	Kln
MG-18 (Talc-bearing)	N35° 54' 46.6'' W05° 22' 35.0''	Whitish schist	xxx	x	x		xx	xxx			x		x	x	x
MG-14 (Talc-free)	N35° 54' 36.4'' W05° 22' 29.1''	Dark-blue phyllite	xxx		x	x	xx	xx	xx	Tr		xxx			
MG-64 (Talc-free)	N35° 52' 09.4'' W05° 23' 08.2''	Black schist	xxx	x		x	xx	xxx				x		?	
MG-62 (Talc-free)	N35° 52' 23.4'' W05° 23' 26.7''	Smoke blue phyllite	xxx	x		x	xx	xxx				xx		?	

xxx: dominant; xx: significant; x: subordinate; Tr: Trace; ?: questionable.

Table 3

Click here to download Table: Table 3.docx

Table 3. Representative and average structural formulae for white mica obtained by SEM/EDX and normalized to $O_{10}(OH)_2$.

	1	2	3	4	5	6	7	8	9	Av. (22)	σ
Si	3.20	3.24	3.25	3.26	3.27	3.28	3.29	3.30	3.32	3.26	0.03
^{IV}Al	0.80	0.76	0.75	0.74	0.73	0.72	0.71	0.70	0.68	0.74	0.03
^{VI}Al	1.48	1.72	1.56	1.66	1.55	1.55	1.59	1.58	1.60	1.59	0.07
Ti	0.05	0.01	0.02	0.01	0.06	0.02	0.02	0.02	0.01	0.03	0.02
Fe^{2+}	0.29	0.11	0.27	0.17	0.22	0.20	0.21	0.18	0.15	0.20	0.06
Mg	0.36	0.20	0.30	0.26	0.33	0.35	0.30	0.32	0.33	0.31	0.04
Σ oct.	2.18	2.05	2.15	2.10	2.16	2.12	2.12	2.11	2.10	2.12	0.03
Ca	0.01	0.00	0.00	0.01	0.00	0.00	0.00	0.01	0.00	0.00	0.00
Na	0.06	0.08	0.04	0.01	0.00	0.03	0.01	0.02	0.01	0.03	0.02
K	0.78	0.84	0.79	0.84	0.74	0.86	0.82	0.84	0.84	0.82	0.03
Σ int.	0.85	0.92	0.83	0.85	0.74	0.89	0.83	0.86	0.86	0.85	0.04

Table 4

Click here to download Table: Table 4.docx

Table 4. Selected and average structural formulae for vermiculite obtained by SEM/EDX and normalized to $O_{10}(OH)_2$.

	1	2	3	4	5	6	7	8	9	10	Av.(25)	σ
Si	2.76	2.84	2.94	2.94	2.97	2.99	3.05	3.08	3.19	3.20	3.06	0.11
^{IV}Al	1.24	1.16	1.06	1.06	1.03	1.01	0.95	0.92	0.81	0.80	0.94	0.11
^{VI}Al	0.69	0.72	0.91	1.06	1.01	1.07	0.99	1.09	1.52	1.17	1.15	0.21
Ti	0.00	0.01	0.01	0.01	0.02	0.00	0.01	0.01	0.01	0.00	0.01	0.01
Fe^{2+}	0.57	0.43	1.07	0.49	0.36	0.42	0.36	0.46	0.26	0.26	0.40	0.16
Mg	1.92	1.86	0.92	1.34	1.33	1.24	1.34	1.11	0.61	1.18	1.05	0.35
Σ oct.	3.18	3.01	2.91	2.90	2.71	2.74	2.70	2.66	2.41	2.60	2.62	0.21
Ca	0.00	0.03	0.04	0.03	0.01	0.00	0.01	0.03	0.02	0.00	0.01	0.01
Na	0.00	0.02	0.05	0.01	0.05	0.00	0.01	0.05	0.04	0.00	0.02	0.02
K	0.19	0.33	0.18	0.12	0.47	0.46	0.49	0.37	0.36	0.43	0.47	0.18
Σ int.	0.19	0.37	0.26	0.15	0.53	0.46	0.52	0.45	0.42	0.43	0.51	0.17

Table 5

Click here to download Table: Table 5.docx

Table 5. Selected and average structural formulae for chlorite/vermiculite mixed-layers obtained by SEM/EDX and normalized to $O_{10}(OH)_4$.

	1	2	3	4	5	6	7	8	9	10	11	12	13	14	15	Av. (33)	σ
Si	3.00	3.07	3.21	3.21	3.24	3.24	3.30	3.35	3.35	3.38	3.45	3.52	3.63	3.69	3.70	3.43	0.23
^{IV}Al	1.00	0.93	0.79	0.79	0.76	0.76	0.70	0.65	0.65	0.62	0.55	0.48	0.37	0.31	0.30	0.57	0.23
^{VI}Al	1.34	1.48	1.50	1.60	1.57	1.57	1.62	1.72	1.66	1.66	1.78	1.79	2.13	2.25	2.24	1.83	0.28
Ti	0.00	0.00	0.00	0.00	0.00	0.00	0.01	0.00	0.00	0.01	0.01	0.00	0.01	0.03	0.00	0.01	0.01
Fe^{2+}	0.72	0.71	0.79	0.72	0.71	0.67	0.72	0.76	0.68	0.74	0.70	0.78	0.63	0.75	0.62	0.70	0.09
Mg	3.70	3.38	3.35	3.23	3.25	3.28	3.12	2.87	3.10	2.96	2.84	2.66	2.26	1.87	2.09	2.73	0.54
Σ oct.	5.76	5.57	5.64	5.55	5.53	5.52	5.47	5.35	5.45	5.37	5.32	5.24	5.03	4.90	4.95	5.26	0.27
Ca	0.00	0.12	0.00	0.02	0.03	0.03	0.03	0.03	0.02	0.04	0.04	0.04	0.04	0.07	0.04	0.03	0.02
Na	0.14	0.05	0.00	0.01	0.06	0.07	0.03	0.04	0.00	0.05	0.03	0.00	0.04	0.02	0.01	0.05	0.04
K	0.00	0.02	0.00	0.02	0.01	0.02	0.04	0.11	0.04	0.06	0.02	0.10	0.03	0.05	0.05	0.09	0.08
Σ int.	0.14	0.18	0.00	0.05	0.10	0.11	0.09	0.19	0.06	0.15	0.09	0.15	0.12	0.14	0.11	0.17	0.09

Table 6

Click here to download Table: Table 6.docx

Table 6. Structural formulae from selected AEM data for chorite/vermiculite (ML), phlogopite (Phl) and vermiculite (Vrm). Structural formulae for mixed-layer was normalized to 25 oxygens. Structural formulae for phlogopite and vermiculite was determinated to 11 oxygens.

	1	2	3	4	5	6	7	8	9	10	11	12	13	14
	ML	ML	ML	ML	ML	Phl	Phl	Vrm	Vrm	Vrm	Vrm	Vrm	Vrm	Vrm
Si	6.46	6.59	6.90	6.66	6.87	2.62	2.83	3.24	3.34	3.39	3.65	3.40	3.52	3.92
^{IV}Al	1.54	1.41	1.10	1.34	1.13	1.38	1.17	0.76	0.66	0.61	0.35	0.60	0.48	0.08
^{VI}Al	2.59	2.49	3.81	2.47	4.64	0.65	0.49	1.88	1.77	1.91	1.69	1.72	1.70	1.69
Ti	0.00	0.00	0.04	0.00	0.00	0.06	0.06	0.04	0.02	0.00	0.03	0.04	0.00	0.02
Fe	1.46	1.45	0.93	1.53	0.57	0.48	0.45	0.12	0.10	0.12	0.10	0.09	0.21	0.10
Mg	4.09	4.19	2.64	4.35	1.67	1.75	1.81	0.21	0.42	0.24	0.33	0.39	0.42	0.26
Σ oct.	8.14	8.12	7.42	8.35	6.88	2.94	2.79	2.25	2.32	2.28	2.16	2.23	2.33	2.07
Ca	0.08	0.08	0.00	0.00	0.00	0.00	0.00	0.00	0.00	0.00	0.00	0.00	0.00	0.00
Na	0.29	0.30	0.30	0.08	0.45	0.04	0.47	0.00	0.05	0.05	0.05	0.00	0.07	0.07
K	0.21	0.21	0.08	0.09	0.28	0.69	0.52	0.30	0.16	0.09	0.22	0.35	0.05	0.14
Σ int.	0.59	0.59	0.38	0.17	0.73	0.73	0.99	0.30	0.21	0.14	0.27	0.35	0.13	0.21

Table 7

Click here to download Table: Table 7.docx

Table 7. Structural formulae for K-rich dioctahedral micas normalized to $O_{10}(OH)_2$ on the basis of AEM data.

	1	2	3	4	5	6	7	8	9	10	11	Av. (11)	σ
Si	3.02	3.13	3.16	3.23	3.20	3.19	3.23	3.18	3.23	3.31	3.03	3.17	0.09
^{IV}Al	0.98	0.87	0.84	0.77	0.80	0.81	0.77	0.82	0.77	0.69	0.97	0.83	0.09
^{VI}Al	1.71	1.58	1.73	1.69	1.74	1.58	1.59	1.69	1.54	1.62	1.66	1.65	0.07
Ti	0.02	0.02	0.02	0.04	0.05	0.00	0.04	0.00	0.00	0.00	0.00	0.02	0.02
Fe	0.11	0.12	0.11	0.12	0.11	0.12	0.11	0.09	0.09	0.09	0.25	0.12	0.04
Mg	0.29	0.48	0.33	0.25	0.25	0.44	0.30	0.39	0.57	0.49	0.43	0.38	0.11
Σ oct.	2.13	2.20	2.19	2.10	2.14	2.14	2.03	2.17	2.20	2.21	2.34	2.17	0.08
Ca	0.00	0.00	0.00	0.00	0.00	0.00	0.00	0.00	0.00	0.00	0.00	0.00	0.00
Na	0.13	0.05	0.11	0.13	0.14	0.18	0.15	0.21	0.11	0.20	0.09	0.14	0.05
K	0.85	0.80	0.60	0.67	0.52	0.76	0.90	0.57	0.71	0.45	0.54	0.67	0.15
Σ int.	0.98	0.86	0.71	0.80	0.67	0.94	1.05	0.78	0.82	0.65	0.63	0.81	0.14

Table

Click here to download Table: Table 2.docx

Table 2. Major (wt.%, XRF) element composition corresponding to Beni Mezala phyllites and other relevant rocks (Sanbagawa data from Izadyar et al., 2000 and Alps data from Chopin, 1981).

	Beni Mezala(18) Talc-bearing	Beni Mezala(14) Talc-free	Beni Mezala(64) Talc-free	Beni Mezala(62) Talc-free	Sanbagawa Talc-bearing	Western Alps Talc-bearing
SiO_2	54.30	55.25	55.25	57.30	71.49	43.71
TiO_2	0.81	0.96	0.90	0.96	0.38	0.34
Al_2O_3	21.89	20.97	22.93	20.97	6.42	24.17
Fe_2O_3	3.79	4.52	6.20	6.87	4.97	
FeO	1.75	3.76	1.95	0.98	0.09	7.08
MnO	0.05	0.01	0.01	0.01	1.52	0.06
MgO	4.54	2.01	1.37	2.01	3.07	14.67
CaO	0.07	1.02	0.14	0.02	2.50	0.21
Na_2O	0.04	1.04	0.01	0.04	1.15	0.16
K_2O	5.77	6.24	7.24	6.24	0.70	2.64
P_2O_5	0.12	0.07	0.14	0.07	0.22	0.29
LOI	6.33	3.56	3.39	3.56	5.95	6.06
Total	99.46	99.41	99.53	99.03	98.46	99.39
Al_2O_3	68.47	67.08	70.66	68.02	44.12	52.64
$FeO+Fe_2O_3$	17.33	26.49	25.12	25.46	34.77	15.42
MgO	14.20	6.43	4.22	6.52	21.10	31.94
$MgO/(FeO+Fe_2O_3)$	0.82	0.24	0.17	0.26	0.61	2.07

Figure
Click here to download high resolution image

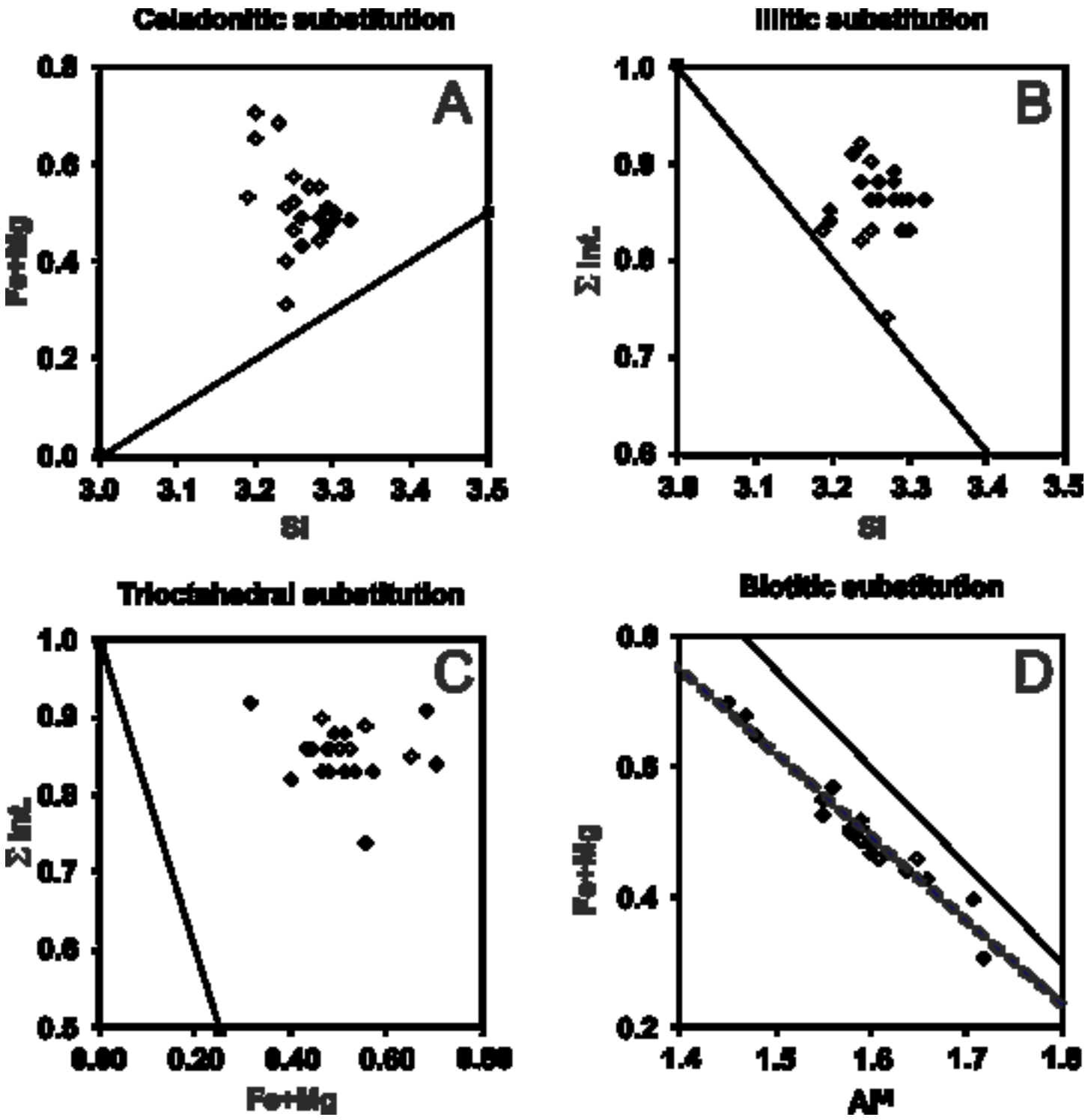

Figure
Click here to download high resolution image

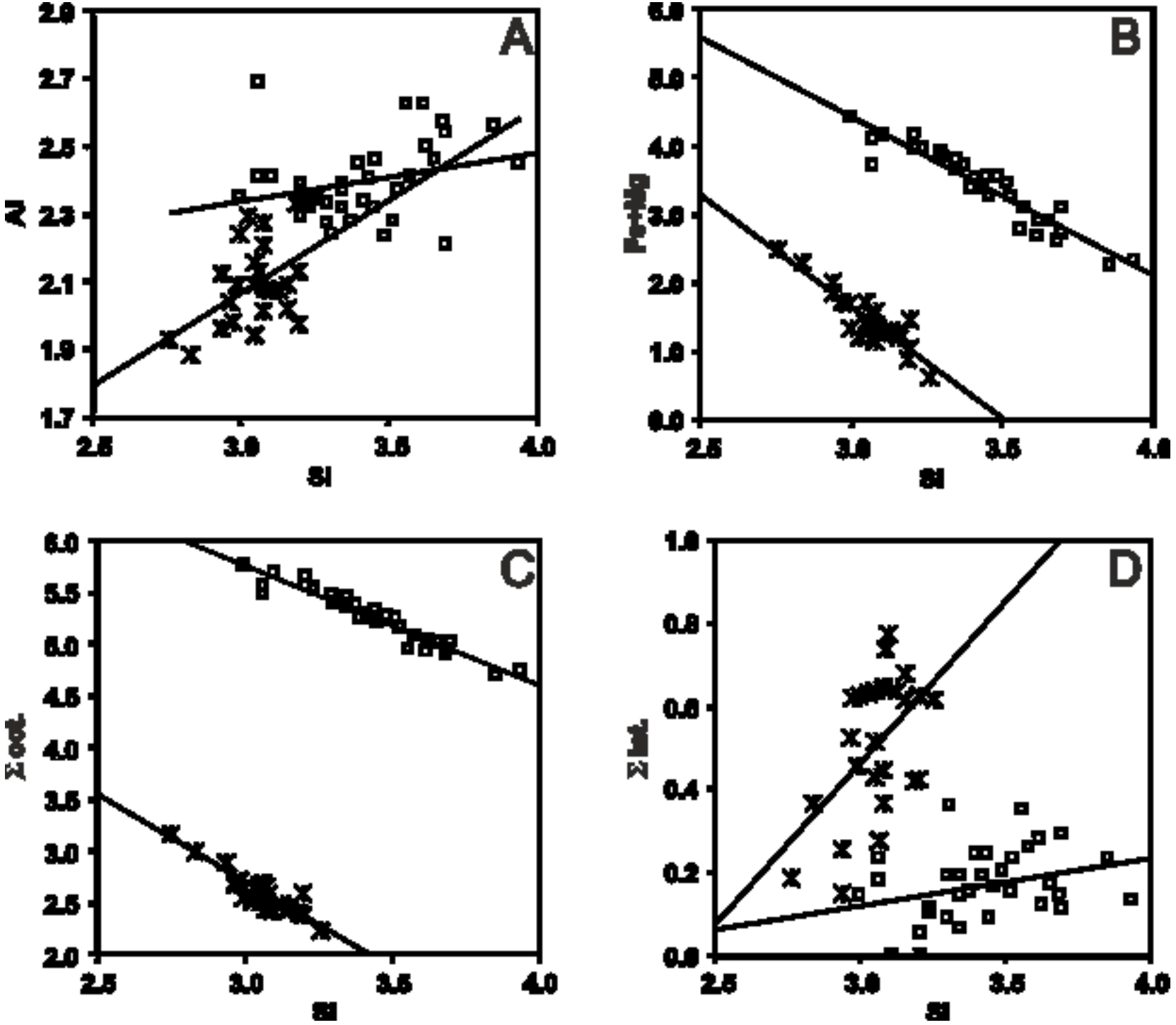

Figure

Click here to download high resolution image

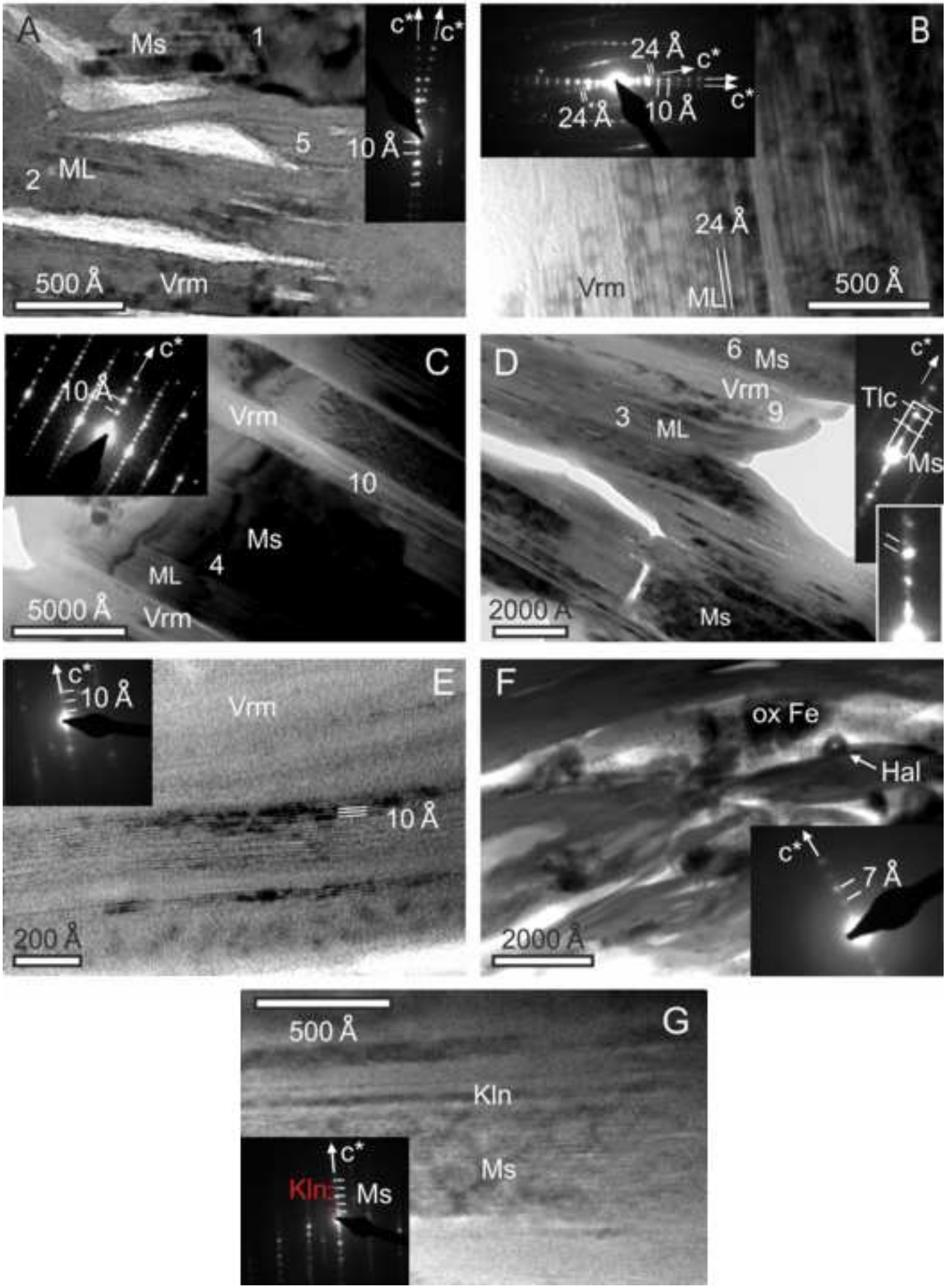

Figure

Click here to download high resolution image

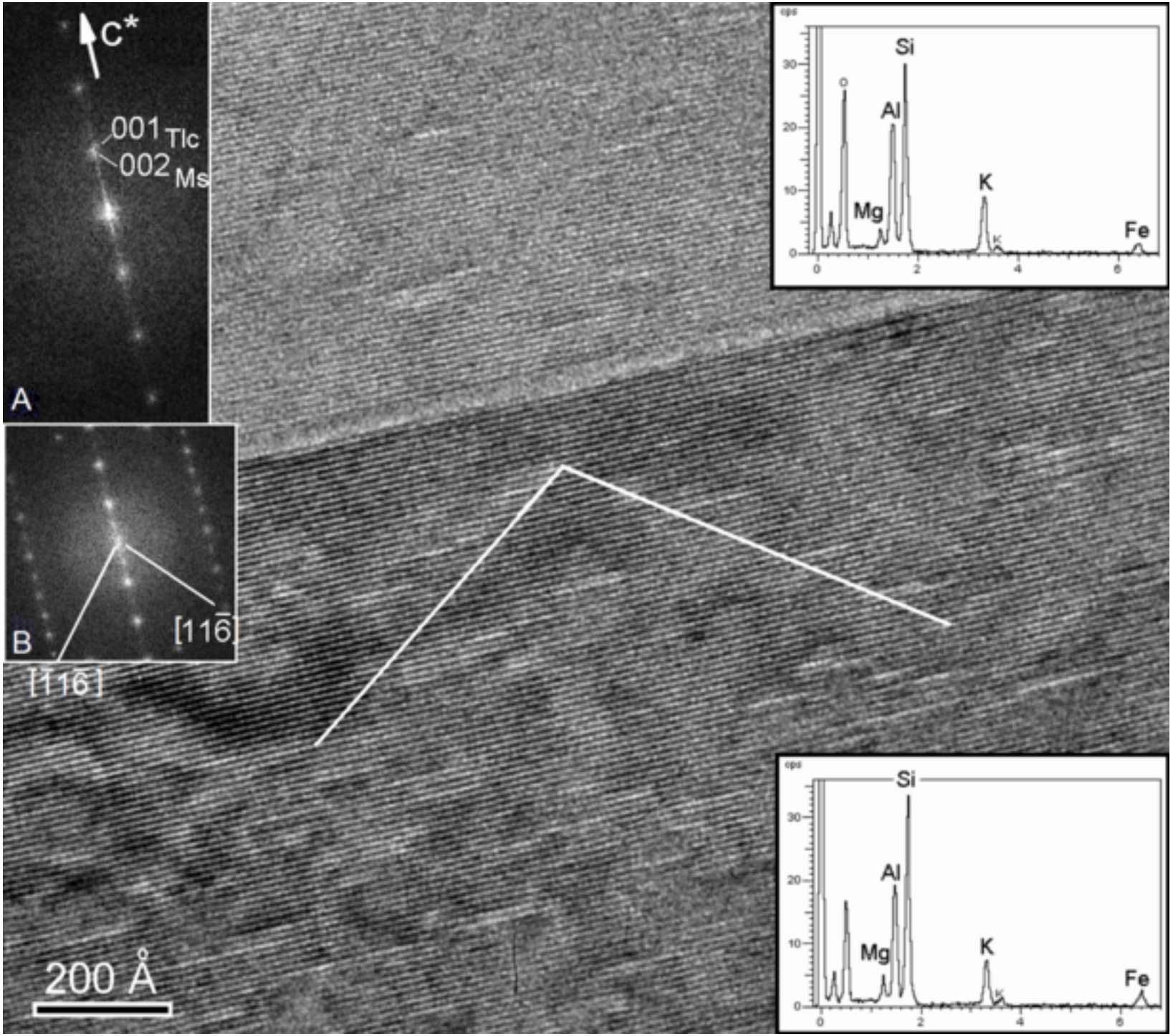

Figure

Click here to download high resolution image

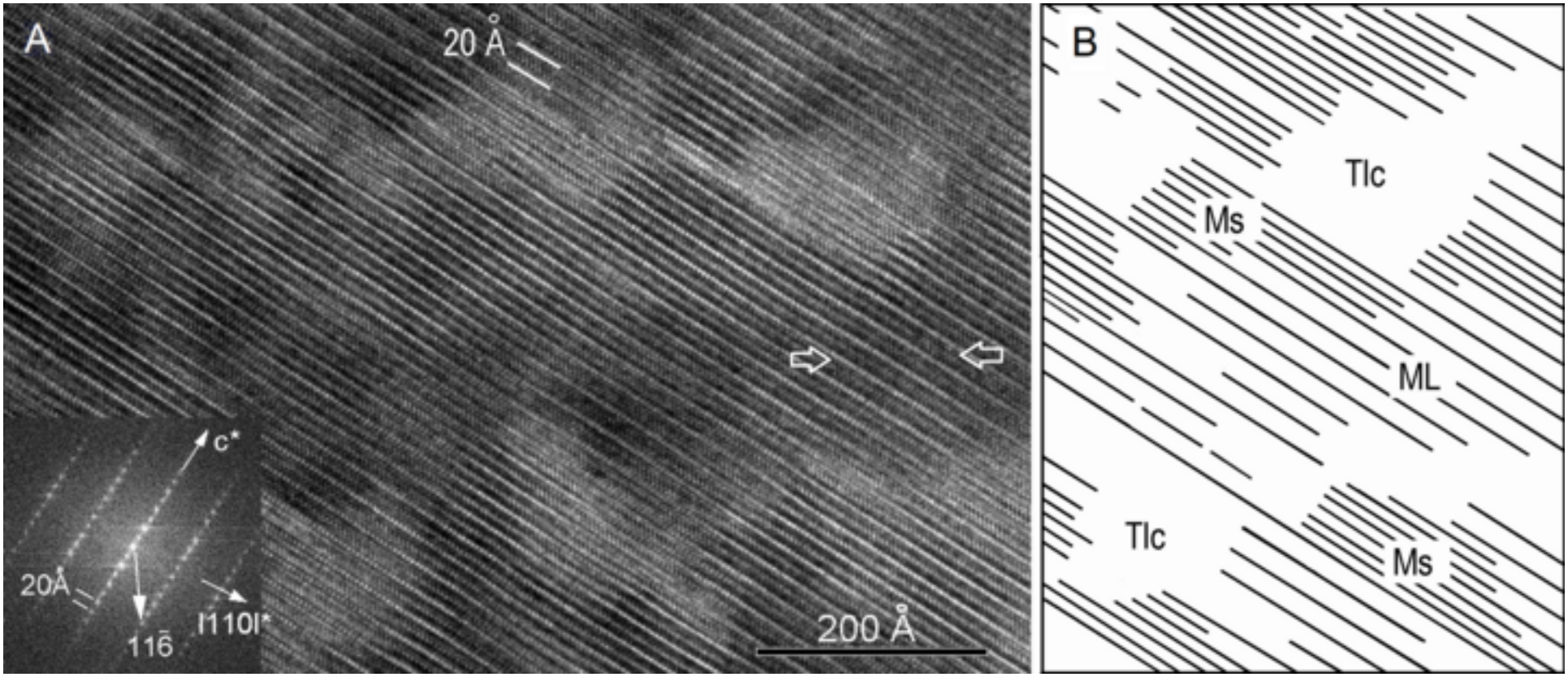

Figure

Click here to download high resolution image

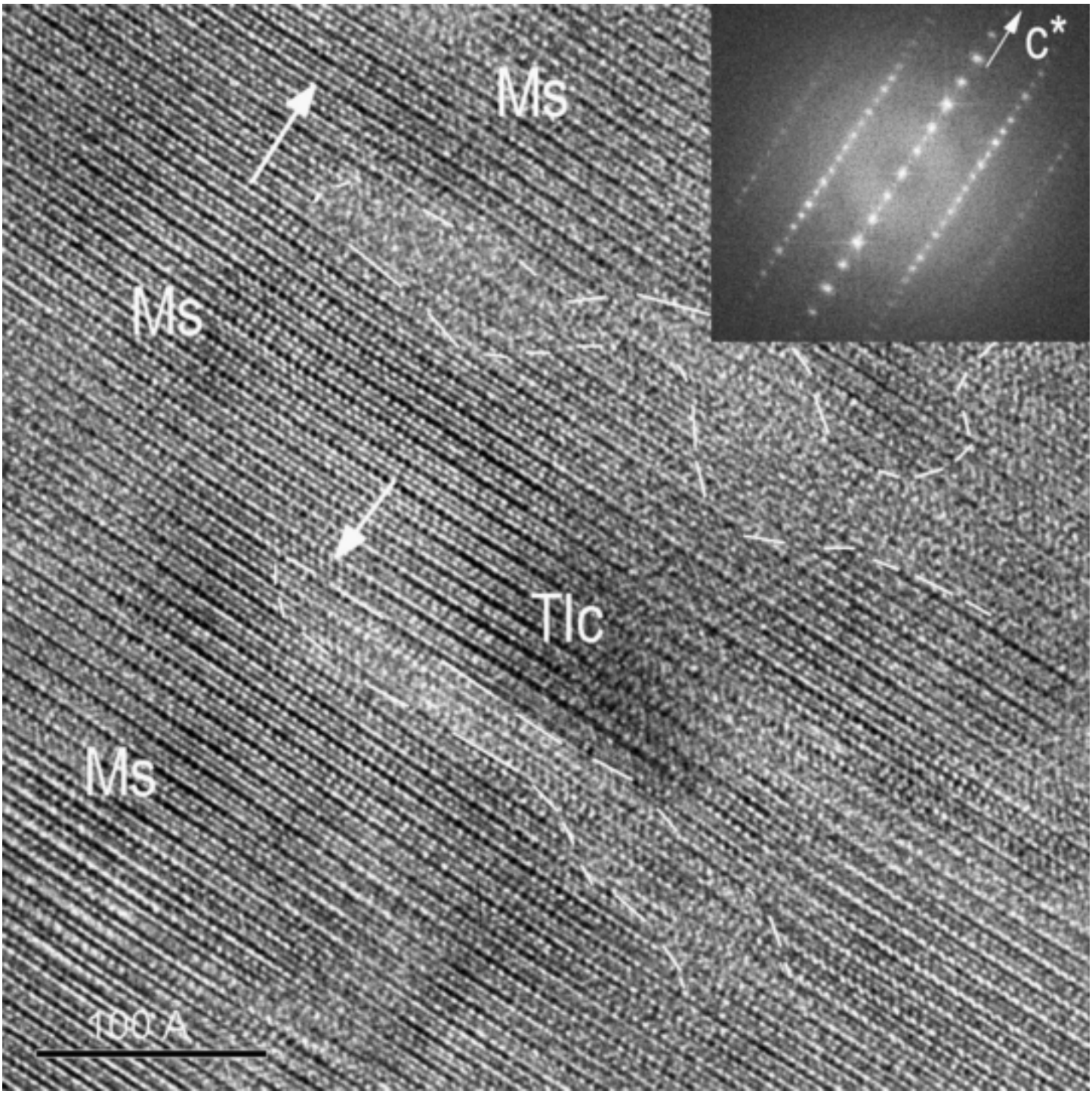

Figure

Click here to download high resolution image

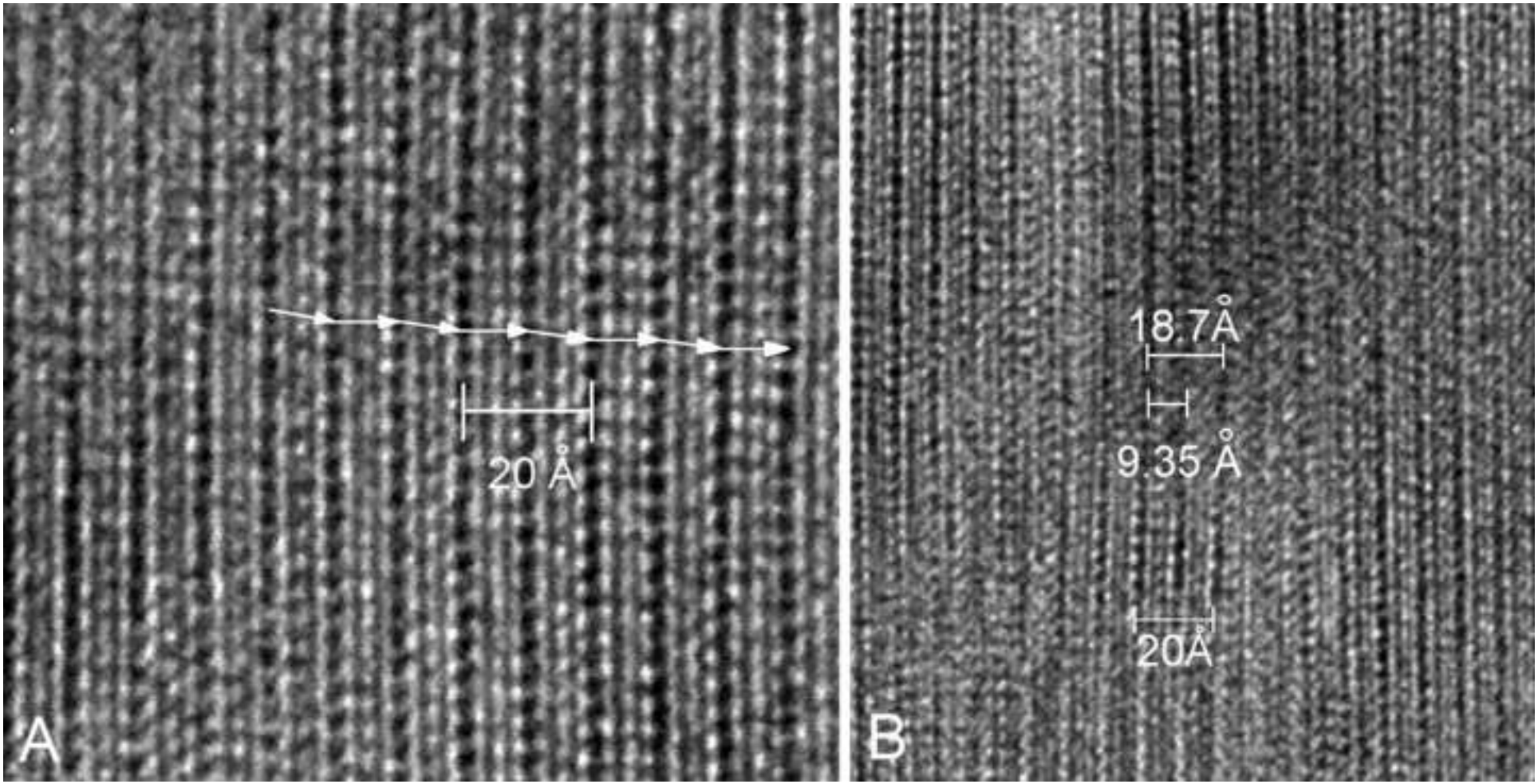

Figure

Click here to download high resolution image

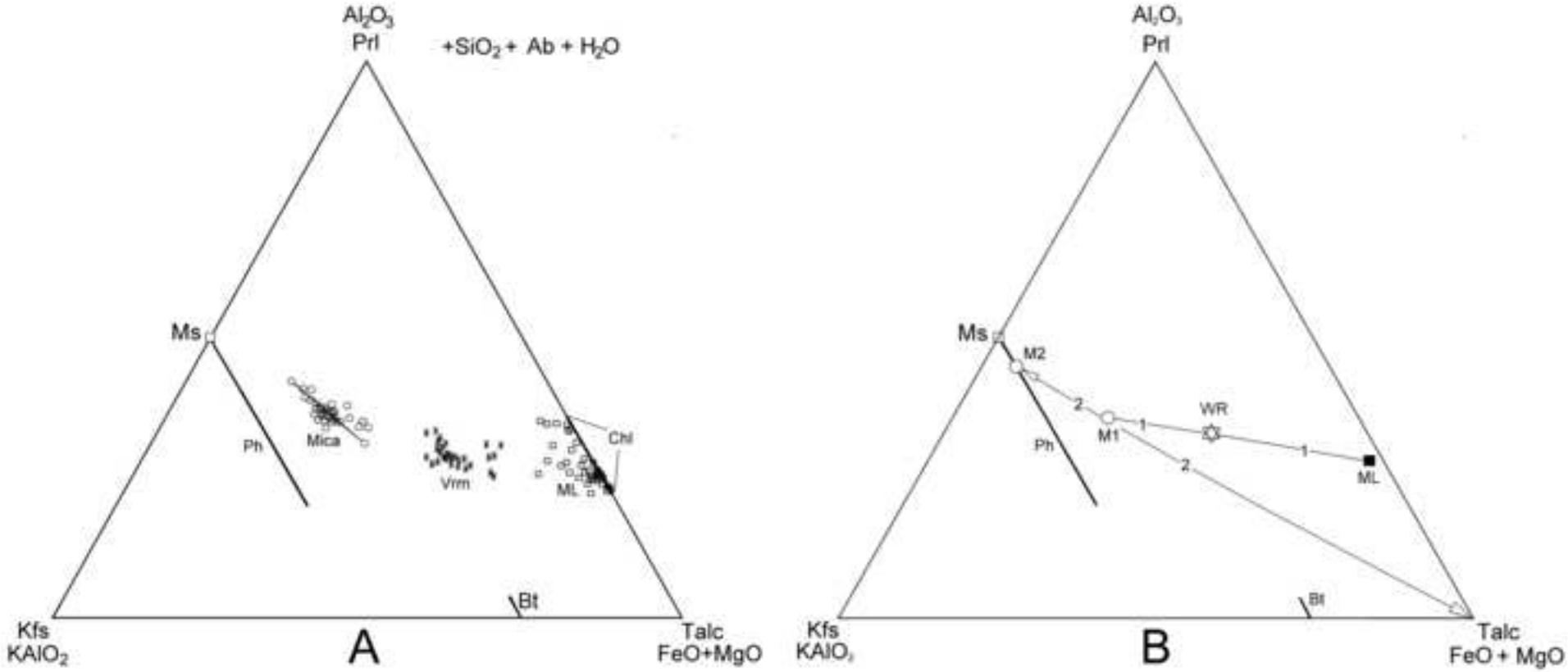

Figure
Click here to download high resolution image

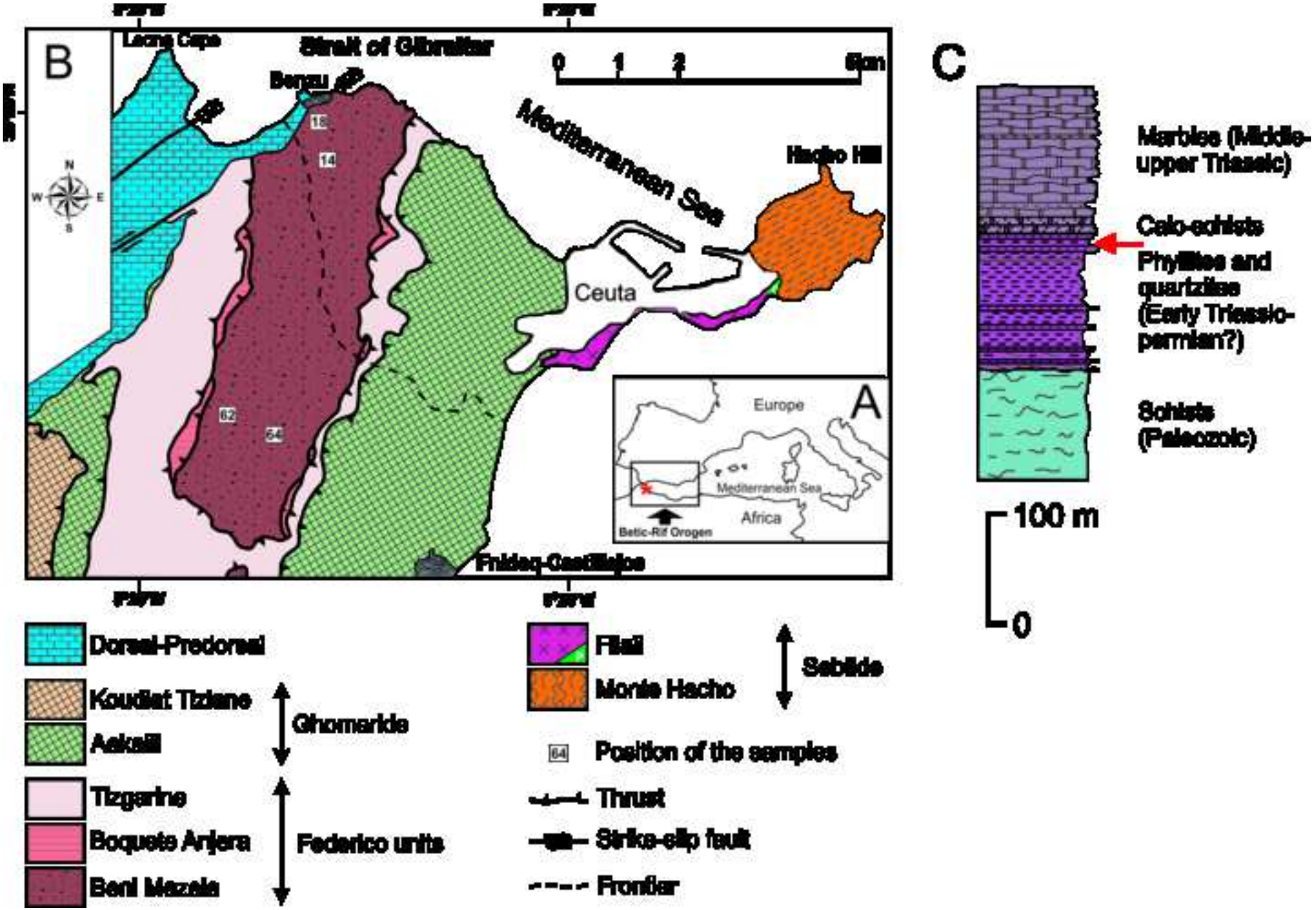

Figure

Click here to download high resolution image